

The emergence of homeostatic epithelial packing and stress dissipation through divisions oriented along the cell long axis.

Tom Wyatt^{1,2,3}, Andrew Harris^{3,4†}, Maxine Lam^{2†}, Qian Cheng⁵, Julien Bellis^{2,6}, Andrea Dimitracopoulos^{1,2}, Alexandre Kabla⁵, Guillaume Charras^{3,7,8^*} and Buzz Baum^{2,8^*}

¹CoMPLEX, Gower St., London WC1E 6BT, UK; ²LMCB, UCL, Gower St., London WC1E 6BT, UK; ³London Centre for Nanotechnology, UCL, 17-19 Gordon St., London, WC1H 0AH, UK; ⁴Bioengineering, University of California Berkeley, Berkeley, CA, USA; ⁵Department of Engineering, University of Cambridge, CB2 1PZ, UK; ⁶Centre de Recherche de Biochimie Macromoléculaire, 1919, Route de Mende, 34293 Montpellier, France; ⁷Department of Cell and Developmental Biology, UCL, Gower St., London, WC1E 6BT, UK; ⁸Institute for the Physics of Living Systems, UCL, Gower St, London, WC1E 6BT, UK

† These authors contributed equally to this work

^ These authors contributed equally to this work

* **For correspondence:** g.charras@ucl.ac.uk; b.baum@ucl.ac.uk

Significance statement

Animal cells undergo a remarkable series of shape changes as they pass through mitosis. The role of mitosis in morphogenetic processes depends strongly on the orientation of division. The cues orienting divisions and the impact of these mitotic shape changes remain poorly understood. Here we use a novel experimental system combining live imaging and mechanical perturbations with computational modeling to investigate the mitotic shape changes in stressed tissues in the absence of neighbor exchange. We show that divisions orient with the cell long axis rather than with the stress direction, and characterise the precise contribution of division to the restoration of cell packing and stress relaxation in morphogenetically active tissues.

Abstract

Cell division plays an important role in animal tissue morphogenesis, which depends, critically, on the orientation of divisions. In isolated adherent cells, the orientation of mitotic spindles is sensitive to interphase cell shape and the direction of extrinsic mechanical forces. In epithelia, the relative importance of these two factors is challenging to assess. To do this, we used suspended monolayers devoid of ECM where divisions become oriented following a stretch, allowing for the regulation and function of epithelial division orientation in stress relaxation to be characterised. Using this system we found that divisions align better with the long, interphase cell axis than with the monolayer stress axis. Nevertheless, since the application of stretch induces a global realignment of interphase long axes along the direction of extension, this is sufficient to bias the orientation of divisions in the direction of stretch. Each division redistributes the mother cell mass along the axis of division. Thus, the global bias in division orientation enables cells to act collectively to redistribute mass along the axis of stretch, helping to return the monolayer to its resting state. Further, this behaviour could be quantitatively reproduced using a model designed to assess the impact of cell autonomous changes in cell mechanics accompanying mitosis on cell shape and stress in a stretched monolayer. In summary, the propensity of cells to divide along their long axis preserves epithelial homeostasis by facilitating both stress relaxation and isotropic growth without the need for cells to read or transduce mechanical signals.

Introduction

The morphogenesis of animal tissues results from coordinated changes in the shape, size and packing of their constituent cells (1-3). These include autonomous cell shape changes (4), the response of cells to extrinsic stresses, and the effects of passive tissue deformation (5). When coordinated across a tissue, these active cellular processes and passive responses enable epithelial sheets to undergo shape changes while retaining relatively normal cell packing (6), and help return tissues to their resting state following a perturbation (7). Although the molecular basis of this cooperation is not understood, several studies have suggested a role for mechanical feedback (8, 9). Cell division has been suggested to participate in this (10) because, in several experimental settings, the rate of animal cell proliferation responds to changes in extrinsic forces (9). Further, division makes an important contribution to tissue morphogenesis in animals (11, 12), accounts for much of the topological disorder observed in epithelia (13), can drive tissue elongation (10), and can facilitate the return to homeostatic cell packing following a deformation (2). Importantly, for each of these functions, the impact of cell division depends critically on the orientation of divisions.

At the cellular level, relatively simple rules appear to govern division orientation. These were first explored by Hertwig, who showed that cells from early embryos divide along their long axis (14), and were further refined using microfabricated chambers (15). However, by following division orientation in cells adhering to micropatterned substrates, more recent studies identified additional roles for both the geometrical arrangement of integrin-mediated cell-substrate adhesions (16) and extrinsic mechanical forces in orienting divisions (17). Consistent with this, adhesive and mechanical cues have been reported to guide division orientation *in vivo* (18) and in epithelial monolayers in developing embryos (12, 19). Nevertheless, the respective roles of cell shape and mechanical tension in guiding division orientation in epithelia remain poorly defined, as does the contribution of oriented division to mechanical feedback control.

Previously, we established suspended epithelial monolayers lacking ECM as a minimal model system in which to study epithelial biology. Since cell divisions in these monolayers become oriented following a stretch, we explored the regulation and function of division orientation. We found that divisions align better with the long, interphase cell axis than with the monolayer stress axis. This phenomenon, combined with the alignment of cellular long axes induced by stretch, results in a global

bias in the orientation of divisions in the direction of extension. Each division redistributes cell mass along the axis of division. Thus, when oriented across a monolayer divisions act collectively to redistribute mass along the axis of stretch, helping to return the monolayer to its resting state. In summary, this analysis shows that the propensity of cells to divide along their long axis preserves epithelial homeostasis by facilitating both stress relaxation and isotropic growth without the need for cells to read or transduce mechanical signals.

Results

Uniaxial monolayer extension results in a sustained cell elongation and tension oriented along the axis of stretch. Previously, we used suspended MDCK monolayers as a model system to study epithelial mechanics (20). For the study of cell division in monolayers, we modified the device (21) to allow imaging over several hours (Fig. S1). Following a stretch, cells in suspended monolayers did not change neighbours (Fig. S2). Instead, they responded by elongating in the direction of stretch by an amount roughly equal to that applied at the monolayer-level (20). Extension was accompanied by a decrease in monolayer thickness (20) and a small decrease in width. Cells then remained elongated until they divided (Fig. 1A,B and S3).

We confirmed that suspended monolayers generated through collagenase treatment (20) were devoid of a continuous load-bearing ECM, but retained apico-basal polarization over the course of our experiments (Fig. S4). Hence, the transmission of tension across suspended monolayers depends entirely on intercellular junctions, which remained stable over the duration of our experiments. To estimate the tension borne by individual cells following stretch, we monitored monolayer tension over 200 minutes. Tension was maximal immediately after deformation before decreasing by 75% within 2 minutes (Fig. 1C). This was followed by a slower but steady decrease in the tension, which remained at ~40 nN/cell for the duration of these experiments (Fig. 1D). When the mechanical integrity of individual cells was perturbed using a pulsed 405 nm laser, we observed a local recoil. To investigate the orientation of stresses at the cellular-scale, we analysed the orientation of this recoil (Fig. 1E-F, S5). In all cases, the local stress field was closely aligned with the axis of stretch, regardless of the orientation of the long axis of the targeted cell (Fig. 1F).

Taken together, these data show that a 30-35% monolayer extension induces a significant change in cell shape and orientation, resulting in an average cell aspect ratio of ~1.4 with 55% of cells oriented within 20° of the stretch axis (Fig 1B). Cells within stretched monolayers were exposed to a sustained local stress that was closely aligned with the extension axis. This resulted in a tension of ~40 nN/cell, several-fold larger than necessary to orient division in adherent cells (17). Thus, cells in stretched monolayers are both elongated and subjected to significant tension, both of which are known to orient cell divisions. Suspended monolayers therefore constitute an ideal system in which to explore the relative importance of force and shape in the orientation of cell division.

The effect of stretch on cell division in suspended monolayers. Mitotic progression within suspended monolayers was visualized using E-cadherin-GFP (Fig. 2A and Video S1). We first explored the timing of divisions. A transient inhibition of mitotic entry was observed following stretch (Fig. S6A), however, mitosis resumed some 60 minutes later. Interestingly, the cells that entered mitosis after this transient delay tended to be those with the largest apical area (Fig. S6B,C) rather than the most elongated – as would have been expected if mitotic entry was triggered by a mechanical cue. These cells then all divided in the plane of the epithelium, as observed for monolayers growing on substrates (22) (Fig. 2A and S7). While cells in non-stretched monolayers divided with no orientational bias (Fig. 2B), a 30-35% strain was sufficient to induce a global bias in the orientation of divisions (Fig. 2B), such that 56% of cells divided within 20° of the stretch axis.

Although previous work has implicated mechanical forces in orienting epithelial cell divisions (19), determining the relative importance of interphase shape and tension is challenging. To do this, we compared the orientation of the stretch axis, the interphase long cell axis and the division axis in the presence and absence of stretch. Cells with a well-defined interphase long cell axis (measured as an aspect ratio, $r > 1.4$) reliably divided along this axis in both stretched and non-stretched monolayers, with respectively $82 \pm 2\%$ and $77 \pm 4\%$ of divisions occurring within 20° of the interphase long cell axis (Fig. 2C). Moreover, mitotic cells were polarized in both stretched and non-stretched monolayers with their spindles aligned with the long cell axis and with known cortical regulators of spindle orientation (Gai and NuMA) concentrated at either pole (Fig S8). To better separate the influence of tension from that of cell shape, we examined the small subset (~5%) of elongated cells, whose interphase long

axis was mis-oriented ($>35^\circ$) with respect to the axis of stretch (Fig. 2D, S3C and Fig. 2C,E, red points). Strikingly, when these cells divided, their divisions were always better aligned with the interphase long cell axis than with the axis of applied stretch (Fig. 2E). This was the case despite these cells being subjected to significant local forces aligned along the global stretch axis (Fig. 1E,F). Taken together these data suggest that the alignment of divisions across a stretched monolayer is the simple result of a stretch-induced global bias in the orientation of long cell axes combined with the propensity of cells to divide along their long axis.

The effect of monolayer stress on mitotic rounding. Next, we investigated the morphological changes accompanying passage through mitosis in cells to assess if changes following a stretch might aid monolayer relaxation (Fig. 2A and Video S1). Within non-stretched monolayers, cells entering mitosis assumed a near isotropic metaphase shape in the plane of the epithelium (aspect ratio, $r_{\text{-stretch}} = 1.16 \pm 0.02$; Fig. 2A and 3A), as do most primary cells and cell lines cultured on ECM (23). By contrast, cells within stretched monolayers were unable to fully round prior to division (aspect ratio, $r_{\text{+stretch}} = 1.25 \pm 0.02$; Fig. 2A and 3A), despite a shortening in their interphase long axis that was larger than observed in non-stretched monolayers (Fig. 3B). *In vitro* measurements show that individual cells generate a rounding force of $\sim 80\text{nN}$ upon entry into mitosis (24). Therefore, the failure of cells to completely round in stretched monolayers is likely a simple consequence of residual monolayer tension ($\sim 40\text{ nN/cell}$, Fig. 1E).

When we measured the evolution of cell dimensions parallel and perpendicular to the axis of division at 5 minute intervals, we found clear differences between cells in non-stretched and stretched monolayers. Cells within non-stretched monolayers retained a roughly constant aspect ratio until anaphase when it increased sharply (ii, Fig 3D). At abscission, the aspect ratio was halved and remained constant over the following 60 minutes (iii, Fig 3D). This behaviour contrasted with that of cells within stretched monolayers, which displayed a marked decrease in aspect ratio upon entry into mitosis (i, Fig 3D), reflecting their more elongated initial shape. Cellular aspect ratio then increased sharply at anaphase before being halved following abscission (ii, Fig 3D). Then, in contrast to non-stretched monolayers, daughter cells underwent a gradual increase in their aspect ratio in the 25 minutes following abscission ((iii), Fig. 3C,D). Daughter cells elongated along the stretch axis regardless of the orientation of division (Fig 3E), implying that it is caused by the extrinsic tension. Overall, these data indicate that extrinsic tension impedes cell rounding at mitotic onset but promotes elongation of daughter cells following division. Surprisingly, cell elongation at anaphase appeared relatively insensitive to extrinsic tension (ii, Fig 3D).

The balance of cell-autonomous and extrinsic mechanical forces explain changes in cell shape accompanying mitotic progression. The clear differences in morphological changes accompanying mitosis between cells in stretched and non-stretched monolayers (Fig. 3) might arise from cross-talk between cell-autonomous changes in cell mechanics during mitosis and extrinsic stresses. To test this hypothesis, we developed a mechanical model to determine how extrinsic stresses influence autonomous shape changes accompanying mitotic progression, the redistribution of cell mass following division, and the likely contribution of oriented divisions to relaxation of monolayer stress.

Cells in the model are represented by linear elastic domains with uniform stiffness calibrated against experimentally measured values (Supplementary information). Stress is balanced by treating the monolayer as a continuous elastic material. While cells can passively slide past each other in response to shear forces along their junctions, cell-cell friction was set high to prevent such rearrangements in this particular implementation to reflect the lack of neighbour exchange in suspended monolayers (Fig S2). Using these assumptions, simulations computed the new monolayer-scale mechanical equilibrium at each time point during division (Fig. 3F). The cell autonomous changes in cell stiffness (represented by a shear modulus G) used to simulate changes in cortical tension accompanying passage through mitosis were derived from measurements in isolated cells (23, 24). A change in cortical (surface) tension ($\Delta\Gamma$) is related to a change in effective shear modulus (ΔG) by $\Delta G = \Delta\Gamma/R$ (where R is the cell radius) (25). To model mitotic progression, we increased stiffness abruptly at mitotic entry (Fig. 3G), kept it constant until division before gradually returning it to interphase levels. At division, cells were forced to divide along their interphase long axis.

Strikingly, although these simulations were based only on experimentally measured autonomous changes in the mechanics of isolated mitotic cells, they yielded changes in the aspect ratios of cells

qualitatively and quantitatively similar to those experimentally observed in monolayers. Thus, the sharp increase in stiffness accompanying entry into mitosis drove complete rounding in control monolayers but only partial rounding in stretched monolayers ((i), Fig. 3H). In addition, while daughter cells in non-stretched monolayers maintained their shape following division ((iii), Fig. 3H), they gradually elongated in the direction of applied stress in stretched monolayers, concomitantly with the return of stiffness to interphase values ((iii), Fig. 3H-G). This suggests that experimentally observed changes in cell shape during division are the simple consequence of well-understood autonomous changes in mitotic cell mechanics, removing the need to invoke additional mechanisms.

Cell division leads to a global redistribution of mass within the monolayer. Next, we investigated the impact of individual cell divisions on local monolayer organisation to understand how oriented divisions may reduce monolayer stress and/or restore cell packing, as previously proposed (19, 26). We examined changes in the shape of dividing cells as well as changes in the organisation of surrounding cells at set time-points during mitotic progression reflecting passage from late G2 into mitosis ($t=-60$ and -50), division ($t=0$), and reintegration into the epithelium ($t=50$ and 60 , Fig. 4A,B, diagrams). This analysis indicated that the net effect of division in both stretched and non-stretched monolayers is to redistribute cell mass along the division axis (Fig. 4A,B). At division, the combined daughter-cell length was larger than mother cell length in late G2 by $35 \pm 3\%$ in stretched monolayers and $37 \pm 4\%$ in non-stretched monolayers (Fig. 4A). 50-60 minutes after division, combined daughter cell lengths had contracted a little but remained significantly longer than mother cell lengths prior to division (by $21 \pm 3\%$ in stretched and $18 \pm 3\%$ in non-stretched monolayers, Fig. 4A). Since width decreased significantly (Fig 4B), the overall effect of division was a significant increase in the aspect ratio of the combined daughter cells compared with their mothers ($+41 \pm 5\%$ in stretched and $+42 \pm 5\%$ in non-stretched monolayers, $p < 0.01$). Qualitatively and quantitatively similar changes in aspect ratio were obtained from simulations with an increase of 29% in stretched and 34% in non-stretched monolayers. Thus, individual divisions lead to the redistribution of mother cell mass along the interphase long axis whether or not the monolayer is under tension.

To determine the effect of division on local epithelial organisation, we compared the position of intercellular junctions close to dividing cells before (green, Fig 4C) and after division (red). Division caused an inward movement of neighbouring junctions in the direction perpendicular to division, together with an outward movement in the direction of division (Fig 4C). Similar patterns of junctional movement were observed in both stretched and non-stretched conditions ($n = 18$), but were absent in control areas of the monolayer where divisions did not occur (Fig. 4C inset and Fig. S9). In summary, each division redistributes mass, which leads to local monolayer expansion along the axis of division and contraction in the perpendicular direction. As there is a global bias in division orientation in stretched monolayers, individual cell divisions act together to expand the monolayer in the direction of stretch and contract it in the perpendicular direction, leading to an overall effect similar to convergent extension.

The effect of monolayer stretch on the orientation of subsequent divisions. To explore how oriented mass redistribution might function over the course of multiple divisions, we then compared the aspect ratio of daughter cells to that of their mothers (Fig. 4D). In non-stretched monolayers, mother cells with an average aspect ratio of $\rho = 1.09 \pm 0.03$ divided to generate daughter cells with an aspect ratio of $\rho = 0.91 \pm 0.02$ (Fig. 4D). Thus, the long axes of mother and daughter cells tend to be perpendicular to one another. By contrast, in stretched monolayers, mother cells ($\rho = 1.34 \pm 0.05$) gave rise to daughters that remained elongated in the same direction ($\rho = 1.10 \pm 0.03$, Fig. 4D). Hence, although division redistributes mass along the division axis in both conditions, the orientation of daughter cells relative to their mothers was altered by stretch. Assuming homogenous cell growth throughout the monolayer, the second round of divisions will tend to be oriented with the first in stretched monolayers, but perpendicular to the first in non-stretched monolayers.

Qualitatively and quantitatively similar results were obtained in the model (Fig. 4E). In stretched monolayers, daughter cells retained the same orientation as their mothers ($\rho = 1.03 \pm 0.03$), whereas in non-stretched monolayers they tended to be oriented perpendicular to the mother cell ($\rho = 0.84 \pm 0.03$). Finally, since the model faithfully replicates the observed cell shape changes accompanying mitosis, we were able to predict the impact of divisions on monolayer stress. In non-stretched monolayers division had no net effect on monolayer stress (Fig. 4F) - as expected under conditions of isotropic monolayer growth. Conversely, in stretched monolayers, divisions along the cellular long axis dissipated monolayer stress whereas divisions perpendicular to it did not (Fig. 4F). Taken

together, these data show how isotropic monolayer growth and the restoration of homeostasis following a stretch can both be understood as emergent properties resulting from the simple ability of cells to orient their division along their interphase long axis.

Discussion

Although it is widely accepted that animal tissues are mechano-sensitive (9), the physical parameters that cells respond to are unclear. This is true even for instances in which an applied force is known to induce a well-defined cellular response. One of the most biologically significant examples of this is oriented cell division - a process that plays a key role in tissue morphogenesis (27) and tissue relaxation (19). However, many aspects of the process remain unclear. For example, it is not known how tissue stress affects the morphological changes accompanying cell division. In addition, since external forces induce stress concomitantly with changes in cell shape, it is challenging to determine the extent to which divisions orient in response to tension and/or cellular deformation. Finally, it is unclear how individual oriented divisions contribute to stress relaxation and tissue homeostasis.

Here, we used suspended epithelial monolayers as a new experimental model to address each of these questions. Several features make suspended monolayers an ideal simplified model. First, in the absence of a continuous substrate, all monolayer-level forces are transmitted across cell-cell junctions. Second, monolayer deformation can be precisely controlled and monolayer-level forces accurately measured over time. Third, cells do not change neighbours during the time-course of experiments relevant to the study of cell division. Following a 30-35% strain, cells in suspended monolayers remained elongated by ~30% along the stretch axis and, simultaneously, experienced a sustained, uniformly oriented tension of ~40 nN/cell. This is ~three-fold higher than the tensions found to orient division in isolated adherent cells (17). After a transient inhibition of mitotic entry induced by stretch, cells with the largest apical areas entered mitosis, before dividing along the stretch axis. These were then used to investigate the relative roles of tension and cell shape in orienting divisions, as well as the function of oriented cell division in the restoration of cell packing and force relaxation following a stretch.

To assess whether the division axis is determined by the stress axis, as recently suggested (17, 19), or by cell shape as suggested by Hertwig and other studies using non-adherent cells from early embryos (14, 15), we focused our attention on the subset of cells whose interphase long axis was mis-oriented relative to the tension axis. Strikingly, these cells divided along their interphase long axis (Fig. 2C-E), even though this differed from the local stress axis (Fig 1E-F). Thus, cell geometry dominates over cellular-level stress in the control of division orientation under the experimental conditions tested here. Consistent with this, the polarization of mitotic cortical markers was aligned with the long cell axis in stretched and non-stretched monolayers. Further, the orientation of division along the long cell axis was as accurate in non-stretched monolayers as in stretched monolayers. Therefore, in suspended monolayers, it is the change in cell shape induced by monolayer extension that dictates the global bias in spindle orientation. It remains to be determined whether this difference with respect to other tissues and adherent cells in culture is related to lack of an ECM (16).

How do individual oriented divisions affect monolayer mechanics in our system? In both conditions, division was accompanied by a marked redistribution of cell mass along the interphase long axis. This appeared triggered by the process of anaphase elongation, which led to lengthening and narrowing of the spatial envelope of the two daughter cells relative to that of the mother cell (Fig. 4A,B and Fig. 5A). This led to a local monolayer expansion along the axis of division and a contraction in the perpendicular direction. Since stretch induces a global reorientation of cellular long axes along the axis of stretch, when summed across the monolayer mass redistribution is expected to facilitate monolayer relaxation. This conclusion was confirmed by numerical simulations based on cell autonomous changes in mitotic cell stiffness; making it clear that our observations can be explained without the need to invoke mechano-sensory signalling. Moreover, the same simulations showed that division only contributes to global stress dissipation when oriented along the long cell axis (Fig. 4D).

Both the experimental data and the model suggest that, in stretched monolayers, mother and daughters will tend to divide in the same orientation over successive divisions until cell shape becomes isotropic (Fig. 4E and 5A), restoring cell packing. In contrast, the orientation of divisions will tend to alternate in non-stretched monolayers, promoting isotropic monolayer growth, as commonly observed in proliferating plant tissues where no neighbour exchange occurs (28).

Taken together, these data suggest a model (Fig. 5) in which mechanical tension operating at the monolayer-scale causes interphase cells to elongate in the direction of stretch. This biases the orientation of cell divisions, which occur along the interphase long axis and redistribute mass to facilitate stress relaxation and the restoration of cell packing over one or multiple rounds of division.

Crucially, this results in a process physically analogous to the stress relaxation induced by passive cell intercalation (29). Thus, stress relaxation through oriented divisions appears to be an emergent property of monolayers that does not require cells to read and interpret other mechanical cues.

Materials and methods

Generation and imaging of suspended monolayers. Suspended monolayers were generated as described in (21). Briefly, stretching devices were built from glass capillaries (Sutter Instruments) and a length of NiTi wire (Euroflex) which acted as a hinge (Fig. S1). Glass coverslips (VWR) on which the cells would grow were glued to the devices. Reconstituted collagen (Cellmatrix) was suspended between the platforms and dehydrated to form a scaffold onto which MDCK cells were seeded. After ~72 hours of culture the collagen was digested and stretch applied with a manual manipulator. Monolayers were imaged with either an inverted spinning disc (Yokogawa) confocal microscope or an FV-1000 scanning laser confocal microscope (Olympus), both with environmentally controlled enclosures. MDCK cells stably expressing Ecadherin-GFP were used for visualizing cell-cell junctions for live imaging and otherwise were fixed in 4% PFA before immunostaining. Image analysis was performed in FIJI (ImageJ) or in custom MATLAB or Mathematica scripts. For more information see SI Methods.

Mechanical model. Cell division was implemented in a force-based computational model. A Voronoi tessellation divides the tissue into cells and forces act on the edges of these polygons. Cells are represented as a strain tensor and interact with other cells through contact force and viscous force. Force balance is applied to each cell to compute the shear forces at cell edges which lead to remodeling. For more information see SI Methods.

Acknowledgements

We thank D. Farquharson and S. Townsend at the UCL workshop, and Joel Jennings and Richard Adams for help with model development. BB and JB thank Cancer Research UK, the BBSRC (BB/K009001), INCa, and M. Piel for funding. TW and AD were supported by the EPSRC. AH was supported by the BBSRC (BB/K013521), and ML by the Agency for Science Technology and Research (Singapore) and Wellcome.

References

1. Farge E (2011) Mechanotransduction in Development. *Forces and tension in development*, ed Labouesse M), 1st Ed Vol 95, pp 243-265.
2. Gibson WT, *et al.* (2011) Control of the mitotic cleavage plane by local epithelial topology. *Cell* 144(3):427-438.
3. Bosveld F, *et al.* (2012) Mechanical control of morphogenesis by Fat/Dachsous/Four-jointed planar cell polarity pathway. *Science (New York, N.Y.)* 336(6082):724-727.
4. Martin AC, Kaschube M, & Wieschaus EF (2009) Pulsed contractions of an actin-myosin network drive apical constriction. *Nature* 457(7228):495-499.
5. Butler LC, *et al.* (2009) Cell shape changes indicate a role for extrinsic tensile forces in *Drosophila* germ-band extension. *Nature cell biology* 11(7):859-864.
6. Treppe X & Fredberg JJ (2011) Plithotaxis and emergent dynamics in collective cellular migration. *Trends in cell biology* 21(11):638-646.
7. Razzell W, Wood W, & Martin P (2014) Recapitulation of morphogenetic cell shape changes enables wound re-epithelialisation. *Development (Cambridge, England)* 141(9):1814-1820.
8. Marinari E, *et al.* (2012) Live-cell delamination counterbalances epithelial growth to limit tissue overcrowding. *Nature* 484(7395):542-545.
9. Streichan SJ, Hoerner CR, Schneidt T, Holzer D, & Hufnagel L (2014) Spatial constraints control cell proliferation in tissues. *Proceedings of the National Academy of Sciences of the United States of America* 111(15):5586-5591.
10. Mao Y, *et al.* (2011) Planar polarization of the atypical myosin Dachs orients cell divisions in *Drosophila*. *Genes & development* 25(2):131-136.

11. Kondo T & Hayashi S (2013) Mitotic cell rounding accelerates epithelial invagination. *Nature* 494(7435):125-129.
12. LeGoff L, Rouault H, & Lecuit T (2013) A global pattern of mechanical stress polarizes cell divisions and cell shape in the growing *Drosophila* wing disc. *Development (Cambridge, England)* 140(19):4051-4059.
13. Gibson MC, Patel AB, Nagpal R, & Perrimon N (2006) The emergence of geometric order in proliferating metazoan epithelia. *Nature* 442(7106):1038-1041.
14. Hertwig O (1893) Ueber den Werth der ersten Furchungszellen für die Organbildung des Embryo. Experimentelle Studien am Frosch- und Tritonei. *Arch. mikr. Anat.* 42:662-807.
15. Minc N, Burgess D, & Chang F (2011) Influence of cell geometry on division-plane positioning. *Cell* 144(3):414-426.
16. They M, *et al.* (2005) The extracellular matrix guides the orientation of the cell division axis. *Nature cell biology* 7(10):947-953.
17. Fink J, *et al.* (2011) External forces control mitotic spindle positioning. *Nature cell biology* 13(7):771-778.
18. Luxenburg C, Pasolli HA, Williams SE, & Fuchs E (2011) Developmental roles for Srf, cortical cytoskeleton and cell shape in epidermal spindle orientation. *Nature cell biology* 13(3):203-214.
19. Campinho P, *et al.* (2013) Tension-oriented cell divisions limit anisotropic tissue tension in epithelial spreading during zebrafish epiboly. *Nature cell biology* 15(12):1405-1414.
20. Harris AR, *et al.* (2012) Characterizing the mechanics of cultured cell monolayers. *Proceedings of the National Academy of Sciences of the United States of America* 109(41):16449-16454.
21. Harris AR, *et al.* (2013) Generating suspended cell monolayers for mechanobiological studies. *Nature protocols* 8(12):2516-2530.
22. Reinsch S & Karsenti E (1994) Orientation of spindle axis and distribution of plasma membrane proteins during cell division in polarized MDCKII cells. *The Journal of cell biology* 126(6):1509-1526.
23. Kunda P & Baum B (2009) The actin cytoskeleton in spindle assembly and positioning. *Trends in cell biology* 19(4):174-179.
24. Stewart MP, *et al.* (2011) Hydrostatic pressure and the actomyosin cortex drive mitotic cell rounding. *Nature* 469(7329):226-230.
25. Weaire D & Hutzler S (2001) *The Physics of Foams* (OUP Oxford) p 260.
26. Ranft J, *et al.* (2010) Fluidization of tissues by cell division and apoptosis. *Proceedings of the National Academy of Sciences of the United States of America* 107(49):20863-20868.
27. da Silva SM & Vincent JP (2007) Oriented cell divisions in the extending germband of *Drosophila*. *Development (Cambridge, England)* 134(17):3049-3054.
28. Green AA, Kennaway JR, Hanna AI, Bangham JA, & Coen E (2010) Genetic control of organ shape and tissue polarity. *PLoS biology* 8(11):e1000537.
29. Keller R (1987) Cell rearrangement in morphogenesis. *Zoological science* 4(5):763-779.

Figure Legends

Fig. 1. Uniaxial stretch results in long-term cellular elongation and monolayer stress. **(A)** E-cadherin-GFP-expressing monolayers before and after a 30% stretch. Scale bars 10 μm . **(B)** The orientation and aspect ratio of cells in stretched (blue) and non-stretched (red) monolayers, as calculated from the orientation and major to minor axis ratio of the best-fit ellipse to the cell shape. **(C-D)** the evolution of strain (grey) and force (black) in a stretched monolayer for short (C, up to 150 s) and long (D, up to 200 min) timescales. **(E)** Ecadherin-GFP expressing cells in a stretched monolayer before and after perturbation of their mechanical integrity by pulsed-UV laser. Cells with shapes oriented $\sim 0^\circ$ (top) and $\sim 90^\circ$ (bottom) to the direction of stretch were chosen. Red dots indicate the area where the laser was applied. Yellow outlines mark the region including the nearest neighbours of the perturbed cell. Scale bars, 10 μm **(F)** The local orientation of stress, as measured from recoil after laser perturbation, for cells with shapes oriented $\sim 0^\circ$ and $\sim 90^\circ$ to the stretch direction. The horizontal line and top and bottom of boxes represent the median, 75th percentile and 25th percentile in all box plots, respectively. The whiskers demark the range. $n \geq 20$ cells, $N \geq 12$ monolayers for each condition.

Fig. 2. Cell divisions align along the long axis of interphase shape in stretched monolayers. **(A)** Time series of a dividing cell, expressing Ecadherin-GFP to enable visualization of intercellular junctions, in a non-stretched and a stretched monolayer. Time is measured from division. Asterisks mark dividing and daughter cells. Scale bars, 10 μm . **(B)** Orientations of divisions w.r.t. the direction of stretch (or w.r.t. the direction perpendicular to the test-rods in the no stretch case). $n \geq 72$ divisions and $N = 3$ monolayers for each condition. **(C)** The orientation of division w.r.t. the axis of stretch (stress, left), to the interphase shape orientation in stretched monolayers (middle), and to the interphase orientation in

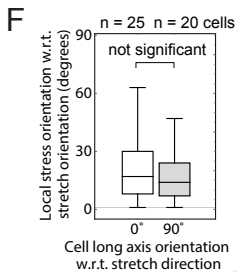
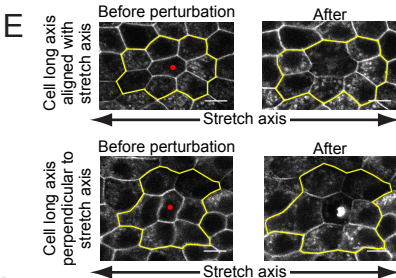
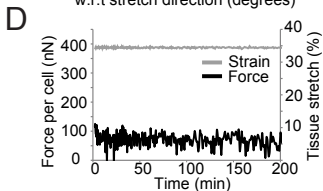
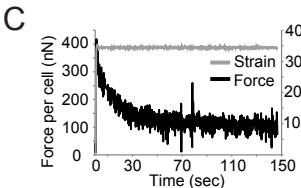
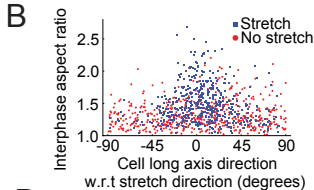
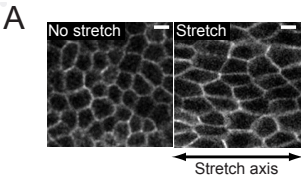
non-stretched monolayers (right) for elongated cells ($r > 1.4$). Cells marked by a red point correspond to those appearing in red in (E). **(D)** A dividing cell in a stretched monolayer. The interphase shape is misaligned with the direction of monolayer stress and the division follows the interphase shape rather than the monolayer stress direction. **(E)** The error in alignment of division with the monolayer stress axes plotted against the error in alignment with the interphase shape for elongated ($r > 1.4$) cells in stretched monolayers. The grey shading shows region in which divisions align equally well with monolayer stress and interphase shape. Dotted lines demark regions where divisions align significantly better with interphase shape than stress and vice versa.

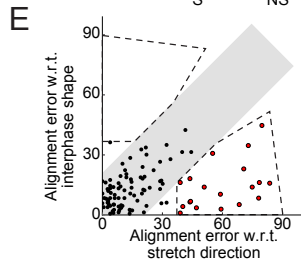
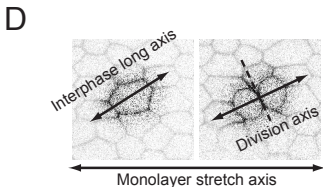
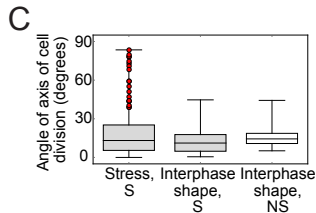
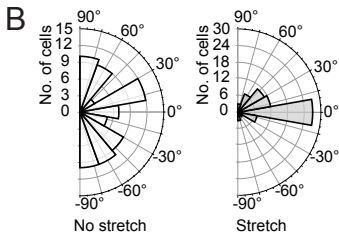
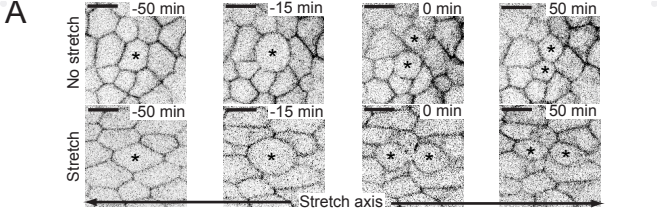
Fig. 3. The effect of monolayer stress on mitotic rounding. **(A)** Box-whisker plots showing the metaphase aspect ratio of dividing cells in non-stretched (NS) and stretched (S) monolayers. $p < 0.002$. The diagrams (top) show the median shape of rounded cells in each condition. **(B)** Changes in the cell long axis length during rounding in non-stretched (NS) and stretched (S) monolayers. The diagrams (top) show the most frequent direction of shape change during rounding in each condition. $n \geq 48$ cells, $N = 3$ monolayers for each condition. $p < 0.001$. **(C)** The change in cell aspect ratio (measured w.r.t. the direction of division) between division ($t = 0$) and $t = 25$ min. $n = 20$ cells for each condition. $p < 0.001$. **(D)** Temporal evolution of the mean cell aspect ratio (measured w.r.t. the direction of division) of dividing cells. Data points are averaged over $n = 10$ cells in both stretched (blue) and non-stretched (red) monolayers. Division was taken as time zero (solid vertical line). Rounding onset (dashed line), anaphase and daughter cell reintegration are marked by (i), (ii) and (iii) respectively and represented by pictograms. From time zero onwards the values represent the average over all individual daughter cells. Error bars indicate standard error. **(E)** The change in cell aspect ratio (measured w.r.t. the direction of division) between division ($t = 0$) and $t = 25$ min for cells without a well-defined long axis ($r < 1.25$) in stretched monolayers. $n \geq 18$ cells were characterized for each condition. $p < 0.001$. **(F)** Example time series of division in a computer simulation of a stretched monolayer. The dividing cell and its daughters are highlighted with red junctions. **(G)** Temporal evolution of cell stiffness during mitosis imposed on all dividing cells in simulations. The times marked with (i), (ii) and (iii) correspond to timings described on panel D. **(H)** Temporal evolution of the mean cell aspect ratio for cells in stretched (blue) and non-stretched (red) monolayers in numerical simulations. Times marked with (i), (ii) and (iii) correspond to the times described for C. Standard error is < 0.02 and so not shown. Each data point represents $n \geq 180$ divisions.

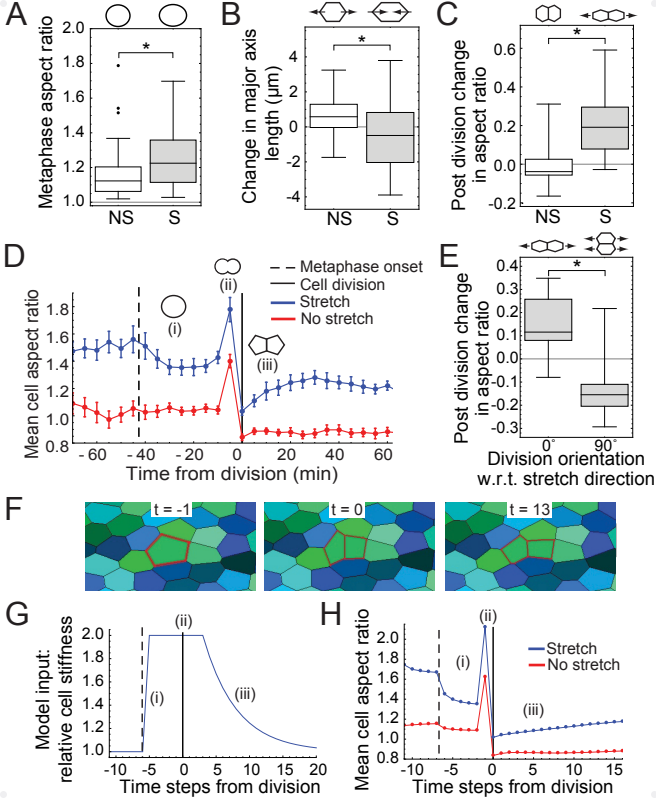
Fig. 4. The effects of stress-induced oriented division on local cell packing and monolayer stress. **(A),(B)** Temporal evolution of **(A)** mean cell length and **(B)** mean cell width of the mother cell (before division) and of the combined spatial envelope of the daughters (after division) in stretched (blue) and non-stretched (red) monolayers showing mass redistribution in the direction of division. Diagrams (top) depict the measurements taken. Asterisks denote a significant difference between medians ($p < 0.01$). $n \geq 38$ cells from $N = 3$ monolayers for each condition. Error bars denote standard error. **(C)** Overlays of mitotic cells 10 minutes before furrowing onset (green) and 30 minutes after (red). Asterisks mark daughter cell and dots mark first neighbours. Fluorescence intensity line profiles taken along the dotted lines show shifts in the position of junctions in cells neighbouring the dividing cell (black arrows in the fluorescence profile). Junctions shift away from the dividing cell along the axis of division (bottom graph) and towards it in the direction perpendicular to division (left graph). No such shifts were observed in overlays of areas containing no division (bottom left). Scale bars $10 \mu\text{m}$. **(D)** The aspect ratio (measured w.r.t. the direction of division) of stretched (S) and non-stretched (NS) cells at 50 min before division (mothers) and 50 min after division (individual daughters). $n \geq 35$ cells and $N = 3$ monolayers for each condition. Diagrams (top) depict measurement taken. Asterisks denote a significant difference between medians ($p < 0.01$). **(E)** The same as (D) but in simulated monolayers. $n \geq 180$ divisions. **(F)** The change in monolayer stress caused by simulated divisions in stretched (S) and non-stretched (NS) monolayers in cases where the division is oriented with the cell shape orientation (oriented) or 90° from it (misoriented). $n \geq 180$ divisions were examined.

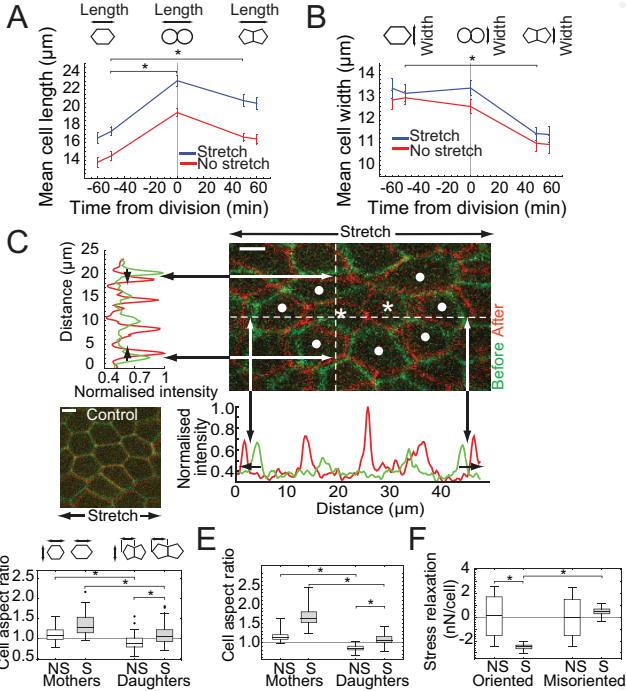
Fig. 5. Epithelial monolayer homeostasis is an emergent property of cell division oriented along the interphase long cell axis. **(A)** A diagram depicting the behaviour of individual cells undergoing division along their long axis in non-stretched and stretched monolayers. Mother cells in stretched monolayers are initially more elongated and fail to round to same extent as cell in the non-stretched control. In both stretched and non-stretched cells, the division orients with cell interphase shape. In non-stretched cells the division creates daughter cells which are oriented approximately orthogonal to the orientation of the mother cell and there is little or no change in shape afterwards. Division in stretched cells creates daughter cells oriented along the same axis as the mother cell. Immediately after

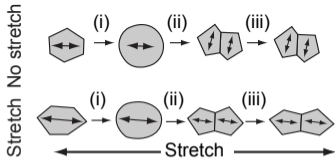
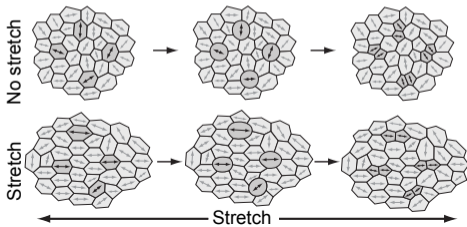
abscission, daughters are approximately isotropic but they then elongate over the following ~25 minutes. The arrows marked with (i), (ii) and (iii) correspond to rounding onset, anaphase and daughter cell reintegration, respectively. **(B)** A diagram depicting the effect of the behaviour in (A) at the monolayer level. The randomly orientated cell shapes in non-stretched monolayers cause divisions to be oriented with a uniform angular distribution so there is no net directional effect. In stretched monolayers, the cell long axes are preferentially aligned with the direction of stretch. Preferential division of cells along their long axes therefore results in a global bias in division in this direction, which is likely to be preserved in consecutive divisions.









A**B**

SI Methods

Cell culture.

Wild-type Madin-Darby Canine Kidney II (MDCK-II) cells were cultured at 37°C in an atmosphere of 5% CO₂ in air in DMEM (Invitrogen, Paisley, UK) supplemented with 10% FCS (Invitrogen) and 1% Penicillin Streptomycin. Cells were passaged at a 1:5 ratio every 3-4 days using standard cell culture protocols and disposed of after 30 passages. For observation and segmentation of cell outlines, we utilised MDCK II cell lines stably expressing E-Cadherin-GFP (described in (1)). MDCK-E-Cadherin-GFP cell lines were cultured in the same conditions as wild-type cells except that 500 ng/ml puromycin was added to the culture medium.

Monolayer extension devices for high resolution long term imaging.

Glass capillaries (Sutter Instruments, inner diameter: 0.5 mm, outer diameter: 1 mm) were bent into shape by heating for several seconds with a micro-pen blowtorch (Gosystem, Cheshire, UK) and forming a right-angle bend using pliers. This was repeated in two positions separated by approximately 20 mm in the centre of the capillary. The capillaries were cut to size with pliers, with one arm long (~34 mm) to act as a rigid reference rod and the other short (~4 mm) to allow for formation of a hinge. A ~8 mm length of NiTi wire of 0.2 to 0.3 mm diameter (Euroflex, Pforzheim, Germany) was dipped in UV curing glue (Loctite Glassbond, Henkel, Cheshire, UK) and threaded into the shorter capillary arm. A second ~30 mm length of capillary was then glued to the free end of the NiTi wire in the same manner. For curing, the glue was exposed to UV light with a UV transilluminator (VWR, Leicestershire, UK) for 5 minutes. Two glass coverslips (VWR) were cut to size (Fig. S1) with a glass scorer and glued to the rods with the same glue. These formed the device test-platforms. At the extremity of the hinged lever, a small section of capillary extends beyond the test-platforms. This served as a notch for moving the hinged arm with a micromanipulator (Fig. S1). Devices were secured into 5 cm plastic Petri dishes (Sterilin, Newport, UK) with plasticine (Blu Tak, Bostik, Leicester, UK).

Monolayer force measurement devices.

Manufacture of force measurement devices is described in detail in (2). Manufacture was similar to the monolayer extension devices except glass capillaries were bent into a U-shape and a flexible test rod composed of a 0.1 mm diameter NiTi wire was threaded and glued into the short arm of the capillaries. Pieces of Tygon tubing were glued to the end of each test rod. Devices were affixed to Petri dishes. Prior to adding the collagen support layer (see 'Suspended monolayer culture'), a small block of PDMS (1 mm wide by 4 mm long) was placed in between the flexible and static rods to keep them at a constant separation until the cells had been seeded.

Suspended monolayer culture.

Suspended monolayers were generated as described in (2) and cultured onto custom-made test-platform devices (created as described in monolayer extension devices, and monolayer force measurement devices). Briefly, collagen type 1A (Cellmatrix, Nitta Gelatin inc., Japan) was reconstituted on

ice in the following proportions: 5 parts collagen, 2 parts water, 2 parts 5X-DMEM (PAA, Colbe, Germany) and one part sterile reconstitution buffer (2.2 g NaHCO₃ in 100 ml of 0.02 N NaOH and 200 mM HEPES). A 16 µl droplet of reconstituted collagen was then deposited between the device test-platforms and remained suspended by capillarity. Devices were placed at 37°C for 90 minutes and allowed to dry giving a thin layer of collagen between the test rods. The collagen support was rehydrated with a 10 µl droplet of DMEM for 30 minutes. This droplet was then removed and an 8 µl droplet of re-suspended cell solution (corresponding to ~40,000 cells) was placed onto the collagen support and incubated at 37°C for 30 minutes. The Petri dishes containing the devices were then filled with 10 ml of culture medium such that the test-platforms were completely submerged. After 48-72 hours of culture, the cells confluenty covered the entire collagen substrate and part of each test-platform. The collagen scaffold was then removed by enzymatic digestion with 250 units/ml of type 2 collagenase solution (Worthington, NJ, USA) in supplemented DMEM solution (Invitrogen, Paisley, UK) for 30 minutes at 37°C. The collagenase solution was then gradually exchanged with supplemented DMEM.

Collagenase removal of basal ECM fibres.

To ensure that all collagen was removed by collagenase treatment, monolayers were immunostained for collagen pre- and post-digestion (see 'Immunostaining of monolayers'). A clear fibrous collagen network was observed pre-digestion whereas no specific staining was found post-digestion (Fig. S4A). Since MDCK cells are known to secrete ECM components (3), we also determined whether any such components were present and whether they would persist after collagenase treatment. We thus immunostained for fibronectin (Fig. S4B) and laminin (Fig. S4C). We observed a weak fibronectin signal on the basal side of the monolayers prior to collagenase treatment that extended several microns in depth but we were unable to detect any basal fibronectin signal after collagenase treatment. A stronger laminin signal was observed on the basal side of monolayers prior to collagen digestion and a fibrous network extending several cell diameters was clearly visible in some areas (Fig. S4C). After collagenase treatment, only small fragments of laminin were detected at the monolayer base. We used automated image analysis (see 'Image analysis of laminin immunostains') to measure the size and shape of the laminin fragments. We found that the area of a laminin fragment was usually much smaller than the area of the cell it was associated with and that the area of the fragment was not correlated with the area of the cell (Fig. S4D). We also found that the elongation (calculated as the ratio of major and minor axes of the best fit ellipse) of the laminin fragment shape was not correlated with the cell elongation (Fig. S4E) and that the orientation of the fragment shape (calculated as the orientation of the best fit ellipse major axis) did not correlate with the orientation of the associated cell (Fig. S4F). We thus concluded that the residual laminin fragments would not be capable of conveying shape information to the cell. Since the laminin was found in isolated fragments rather than a continuous network, the remaining laminin would not be capable of transmitting stress across the monolayer.

Image analysis of laminin immunostains.

Confocal stacks of laminin immunostaining in the area of interest were combined with a maximum intensity projection and thresholded to create a binary image. For each image the threshold was chosen via comparison to maximum intensity projection of an equivalent region outside the area of interest from the same image stack (i.e. an area which contained no signal so was composed solely of noise). The threshold was then chosen such that 10% of the pixels in this 'noise image' were converted to white by thresholding. By guaranteeing a constant fraction of noise in each threshold image, this ensured that the dimensions and connectivity of laminin fragments was not underestimated. The binary images were then processed with a morphological opening and closing and Laminin fragments were defined as connected components of the resulting images. All image analysis was performed in Mathematica (Wolfram Research, Inc., Champaign, IL., USA).

Exposing monolayers to defined extensions.

Monolayers cultured on extension devices were extended as described in (2). Briefly, a steel wire (0.7 mm diameter) was bent into an L-shape and one extremity was positioned between the test-platforms and used to prise them apart with a micromanipulator. The position of the wire was then secured to the edge of the Petri dish using hot-glue.

Stress relaxation measurements.

Stress relaxation measurements were carried out as described in (1) and utilised force measurement devices (see 'force measurement device fabrication'). Briefly, a motorised micromanipulator (Physiks instrumente, M126DG1 stage and C863 controller) was used to subject the monolayers to stretch. Deflection of the flexible wire was imaged with a top down microscope consisting of a macrolens (Canon FD) interfaced to an EMCCD camera (Hamamatsu ORCA ER). Monolayer strain was held constant by altering the force applied with custom feedback routines implemented in LabView (National Instruments, Austin, Texas, USA). Measurements were effected in a temperature controlled enclosure at 37°C. To prevent evaporation, a small layer of mineral oil (Sigma) was deposited on top of the medium. For stress relaxation measurements the stepper motor was driven 0.4 mm at a speed of 1 mm/s (~100%/s) up to a target strain of ~35% (1).

Live imaging of monolayers.

For live cell imaging, an inverted spinning disc confocal microscope equipped with an environmentally controlled enclosure was utilised. The spinning disc confocal consisted of a Yokogawa spinning disk head (Yokogawa, CSU22) and an iXon camera (Andor, Belfast, UK). iQ software (Andor) was used for acquisition. Both Olympus 30x NA 1.05 silicone oil immersion and Olympus 60x NA 1.2 water immersion objectives were used. For imaging with an inverted microscope, the extending devices were transferred to glass bottomed petri dishes (Intracell, Herts, UK) where they were secured with hot glue. Measurements were performed at 37°C, 5% CO₂ and a humidified atmosphere. Confocal z-stacks comprising ~20 planes spaced ~1.5 μm apart were acquired at regular 5 min intervals for up to 4h.

Determination of cell shape and the angle of division.

Confocal images of monolayers were automatically segmented and hand-corrected using Packing Analyzer, v2.0 (4). For measurements of cell shape, the best fit ellipse of the cell outline was calculated in FIJI (5) and the ratio of ellipse major axis over minor axis was used as a measure of cell aspect ratio and the ellipse orientation as cell orientation. For the orientation of division, the angle of the new junction formed between daughter cells was measured at the first time-point that it was visible. The orientation of the division was then assigned as the angle perpendicular to this direction. For measurements of cell dimension in the direction parallel and perpendicular to division, the dimensions of the cell segmentation bounding box oriented with respect to the division axis was calculated in FIJI.

Laser perturbation of monolayers.

Suspended and stretched monolayers were prepared using Ecadherin-GFP expressing MDCK cells in order to visualize the junctions. Hoechst-34332 (5 µg/ml) was added in order to visualize nuclei. For each perturbation, a cell with an elongated shape either in the direction of stretch or in a direction perpendicular to stretch was identified and a confocal image stack containing the cell and its neighbours was obtained. A small region in the nucleus of the cell was then exposed to a pulsed 405 nm laser (PicoQuant, Berlin, Germany) and a 405 nm laser (Olympus, Berlin, Germany) for 30 seconds piloted through an FV-1000 scanning laser confocal microscope (Olympus, Berlin, Germany). A confocal stack, equivalent to the first stack, was then obtained 5 minutes after the laser perturbation. The time difference of 5 minutes was identified as a characteristic timescale on which an elongation of the patch after perturbation was observed.

Determining local stress direction from laser perturbations.

For each perturbation, the outline of the patch defined by the perturbed cell and its neighbours was traced manually and converted into a binary mask in FIJI. A mask representing the cells before perturbation (mask A) and after perturbation (mask B) was created in this manner. The centroid of each mask was placed at the centre of the image. A transformation ($T(\theta, m, n)$) was applied to mask A, representing an elongation of size m of the mask, in a direction oriented at angle θ to the direction of the applied monolayer stretch and an elongation of size n in the direction orthogonal to θ . The transformation origin was set to the centre of the image. The transformation T was formed from the combination of the stretch transformation matrix $S(m, n)$ and the rotation transformation matrix $R(\theta)$ as:

$$T(\theta, m, n) = R(\theta)S(m, n)R(-\theta),$$

where

$$S(m, n) = \begin{pmatrix} m & 0 \\ 0 & n \end{pmatrix}$$

and

$$R(\theta) = \begin{pmatrix} \cos \theta & -\sin \theta \\ \sin \theta & \cos \theta \end{pmatrix}.$$

A measure of how closely the transformed mask A matched mask B was then calculated by overlaying the two masks and summing the pixels which were white in *both* masks and normalising by the sum of pixels which were white in *either* mask. The transformation of mask A which produced the best match of mask B was then identified using this measure. The angle θ was then taken as an approximate measure of the orientation of local stress in the tissue.

Immunostaining of monolayers.

For immunostaining of ECM components the monolayers were stained live, either before or after collagenase treatment. Fixing and permeabilisation was not necessary since only extracellular components were of interest. The monolayers were affixed to glass bottom petri dishes and washed in PBS. They were then incubated at 37°C, 5% CO₂ for 30 minutes with either monoclonal mouse anticollagen antibody (Sigma Aldrich, Gillingham, UK, dilution: 1:100), polyclonal rabbit antifibronectin antibody (Abcam, Cambridge, UK, dilution: 1:200) or polyclonal rabbit antilaminin (Sigma Aldrich, dilution: 1:25). Primary antibodies were diluted in unsupplemented DMEM. Monolayers then were incubated for 30 minutes with either Alexa Fluor 647 goat anti-mouse (Invitrogen, Paisley, UK, dilution 1:100) or Alexa Fluor 568 goat anti-rabbit (Life Technologies, dilution 1:100), in DMEM supplemented with 10% FCS. Monolayers were then washed in DMEM and imaged immediately. For all other immunostains monolayers were pre-extracted in a PHEM buffer (60mM PIPES, 25mM HEPES, 10 mM EGTA, 2mM MgCl₂, pH 6.9) containing 1% Triton X-100 for 1 min, fixed with 4% formaldehyde in PHEM buffer for 20 min, permeabilised for 30 min in PHEM buffer with 0.5% Triton X-100, blocked for 30 min in 0.05% BSA-PBS, and incubated overnight with primary antibodies. Following primary staining, monolayers were incubated for 6 hours with secondary antibodies as well as DAPI and Phalloidin-TRITC to label nucleic acids and F-actin respectively.

Quantification of cortical polarisation orientation w.r.t. cell long axis orientation.

Quantification of cortical protein polarisation with respect to the cell long axis (Fig. S8E) was performed using custom MATLAB scripts, consisting of image analysis and signal processing of single confocal image slices. Firstly, the spindle coordinates were manually detected based on NuMA localisation at the two spindle poles. From these coordinates, the spindle centre was calculated. For each cell of interest, the cell edge was then segmented using the F-actin channel. For this, the XY image was converted to a polar coordinate system with r the radial distance from the cell spindle centre and θ the angle from the horizontal (Fig. S8E). The cell boundary was then detected by applying an edge detection filter. The edges closest to the cell centre were then smoothed producing a clear segmentation of the cell edge that was then manually validated. Thirdly, a band between 1 and 3 μm thick (depending on the cell) centred on the coordinates of the segmented actin was extracted from the NuMA and Gai channels (Fig. S8E). From these bands, the maximum intensity was calculated for each angle θ . From the segmentation of the cell edge we also obtained the diameter of the cell as a function of θ , which corresponds to the edge to edge distance passing through the spindle

centre at a given angle from 0 to 360 degrees. From these data, we were able to obtain the orientation of the cell long axis that we used as reference for further analysis. Finally, using a circular convolution algorithm, the cross-correlation between the length of the cell diameter and the fluorescence intensity of protein signals at the cortex was calculated. This enabled us to estimate the NuMA and Gai polarisation with respect to the cell long axis (Fig. S8F).

Mechanical model.

A force-based computational model, described in (6) was used. Briefly, a Voronoi tessellation divides the tissue into polygons associated with each cell and forces can act on the edges of each polygon, which define the shape of the cell and its interfaces with neighbouring cells. Cells are represented as a strain tensor and exhibit viscoelastic behaviour under shear stress. Cells interact with other cells through contact force and viscous force. The contact forces act normal to the interface between cells. Viscous force occurs when cells move relative to each other. The model uses a linearly elastic constitutive relationship between the stress and strain of the cell (with a shear and bulk modulus as parameters). Force balance on each cell is then used to compute the required shear forces at the cell interfaces, leading to the remodelling and sliding of cells past each other, with a rate controlled by an interfacial viscosity. The resulting partial differential equations (PDE) are used to update the stresses and positions of each cell within the tissue. Oriented division is implemented by introducing a new edge which divides the mother cell into two identical daughter cells. The new edge is by default perpendicular to the mother's main axis of elongation. In the present study, cell rearrangements in response to the stretch are not observed and we selected a high value for the interfacial viscosity so that the relaxation time by cell rearrangement is large compared to the simulation time. The key parameters controlling the tissue behaviour during cell division is the relative increase of the stiffness of the dividing cells.

SI Figure Legends

Fig. S1. Diagrams of the suspended monolayer extension devices pre- and post-stretch along with bright field images at various stages of the experiment (inset). Scale bars 1 mm.

Fig. S2. No neighbour exchange occurs in suspended stretched monolayers. **(A)** A monolayer immediately before (left) and 15 minutes after (middle) application of stretch along with the before/after overlay (right). MDCK cells stably expressing E-Cadherin-GFP were mixed with wild-type cells in a 1:1 ratio to produce a monolayer which consisted of patches of both cell types. This allowed comparison of groups of cells before and after stretch and enabled identification of neighbour exchange events. We could detect no such events following application of stretch. Arrowheads point to corresponding points of reference between the two images. Scale bars 20 μm . **(B)** Confocal images of two sections of a stretched MDCK monolayer stably expressing E-Cadherin-GFP, at three time-points after application of stretch. In the first

section (top) two cells divide (red asterisks) whereas no cells divide in the second section (bottom). In each section, several cells are marked with white asterisks to serve as fiducial markers to aid comparison of the tissue organisation over time. Despite significant changes in cell shape in the vicinity of dividing cells, we observed no significant neighbour exchange events over time periods of > 2 hours. Scale bars 10 μm .

Fig. S3. Cell shape in stretched and non-stretched monolayers. **(A)** The distribution of the interphase cell shape orientation with respect to the stretch axis in stretched (blue) and non-stretched (red) monolayers. **(B)** The distribution of interphase aspect ratios in stretched (blue) and non-stretched (red) monolayers. **(C)** Examples of cells before stretch, immediately after a 30% stretch and after 1 hour of a sustained 30% stretch. The top panel shows a cell whose long axis is oriented with the direction of stretch, while the bottom panel shows a cell whose long axis remains oriented perpendicular to the stretch axis as a result of its initial shape. Yellow bars show the cell long axes. Scale bars 10 μm .

Fig. S4. Collagenase removal of basal ECM fibres. **(A)** XY (above) and XZ (below) projections of monolayers made from MDCK cells expressing Ecadherin-GFP (green) stained for collagen (red) before and after collagenase treatment. Images show a representative example from $n = 27$ images taken from $N = 3$ monolayers. Scale bars 15 μm . **(B)** The same as in (A) but staining for fibronectin (red). **(C)** The same as in (A) but staining for laminin (red). **(D)** The area of the laminin fragments found on the basal side of the monolayer compared with the area of the cells they are associated with. Fragments analysed from $n = 6$ images from $N = 3$ monolayers. **(E)** The elongation of the laminin fragments found on the basal side of the monolayer compared with the elongation of the cells they are associated with. **(F)** A histogram of the difference in orientation of each laminin fragment compared with the cell it is associated with.

Fig. S5. Obtaining a measure of local monolayer stress from laser perturbations. **(A)** Images of MDCK cells expressing Ecadherin-GFP in stretched suspended monolayers just before and 5 minutes after laser perturbation. The red dots mark the location exposed to the laser. The yellow lines mark the manually traced outline of the perturbed cell and its nearest neighbours. Scale bars, 10 μm . **(B)** Binary masks were obtained from the outlines shown in yellow in (A). The mask of the 'before' image was stretched by independent factors (m and n) along orthogonal axes (x' and y') oriented an angle θ from the direction of applied stretch. The bottom left panel shows a such a transformation applied to the 'before' image using $m = 1.15$, $n = 1.05$ and $\theta = 5^\circ$. The bottom right panel shows a difference image composed from an overlay of the transformed 'before' mask and the 'after' mask which is used to assess the closeness of the fit. It is created by converting each pixel which is different in the two masks to white and setting all other pixels to black (picture grey).

Fig. S6. An applied tissue stress transiently inhibits mitotic entry. **(A)** Cumulative frequency graph showing the fraction of cells that entered mitosis

from 100 min before application of stretch to 300 min after. Stretch was applied at time $t = 0$ min. Monolayers consisted of MDCK cells stably expressing E-Cadherin-GFP and mitotic cells were identified based on their rounded morphology. Experiments were carried out in the presence of 50 μM STLC to cause mitotic arrest. In total $n = 344$ cells had entered mitosis by the final time point representing 3% of the cells in the fields of view examined. Error bars represent standard deviations from $N = 5$ monolayers. **(B)** Box-whisker plot comparing the aspect ratio of cells which do and do not divide in stretched and non-stretched monolayers. The horizontal line and top and bottom of boxes represent the median, 75th percentile and 25th percentile in all box plots, respectively. The whiskers demark the range and the dots are outliers. # denotes a non-significant difference between means ($p > 0.6$). **(C)** Box-whisker plot comparing the area of cells which do and do not divide in stretched and non-stretched monolayers. * denotes a significant difference between means ($p < 0.01$). In (B) and (C) $N = 3$ monolayers were examined for each condition and the total number of cells in each case (n) is given.

Fig. S7. Spindles orient parallel to the plane of the epithelium in stretched monolayers. A lateral view of a monolayer fixed 3 hours after stretch and stained for DAPI (grey), alpha-tubulin (green), actin (red) and E-cadherin (magenta). The spindle is aligned parallel to the plane of the epithelium as shown by the dotted line encompassing the two spindle poles. Scale bar 10 μm .

Fig. S8. The metaphase cortex is polarised in stretched and non stretched cells. **(A)** An apical view of a monolayer fixed 3 hours after collagenase treatment and stained for DNA (grey), NuMA (magenta), actin (red) and $G\alpha_i$ (green). The arrows highlight polarised NuMA and $G\alpha_i$ localization. Scale bars 5 μm . **(B)** The same as in (A) but in a monolayer that was stretched by 30% immediately after collagenase treatment. **(C)** Box-whisker plots showing the orientation of NuMA polarization w.r.t. the cell shape orientation, in immunostains of stretched (S) and non-stretched (NS) monolayers. The horizontal line and top and bottom of boxes represent the median, 75th percentile and 25th percentile in all box plots, respectively. The whiskers demark the range. $n \geq 17$ cells in $N \geq 4$ monolayers. **(D)** Box-whisker plots showing the orientation of $G\alpha_i$ polarisation w.r.t. the cell shape orientation, in immunostainings of stretched (S) and non-stretched (NS) monolayers. $n \geq 17$ cells in $N \geq 4$ monolayers. **(E)** Measures of the orientation of the cell shape and cortical polarization were obtained via automated image analysis of the immunostains (see SI methods). Each channel was polar projected (middle panels) and the cell outline was automatically segmented from the actin channel (yellow line). From this, the distance from the spindle centre to the cell edge could be calculated for each angle (lower plot) and the NuMA and $G\alpha_i$ cortical signals could be extracted (yellow lines, middle panels). **(F)** The alignment of the cortical polarisation with the cell shape was calculated from the cross-correlation of the extracted NuMA or $G\alpha_i$ signal with the actin signal.

Fig. S9. A control overlay. An overlay in a region of tissue stretched monolayer where divisions do not take place between time points 0 minutes

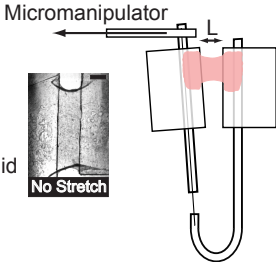
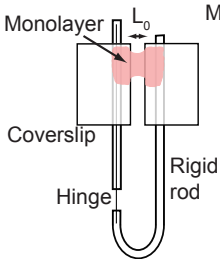
(green) and 40 minutes (red). Fluorescence intensity line profiles measured along the dotted white lines show that there is little junctional movement.

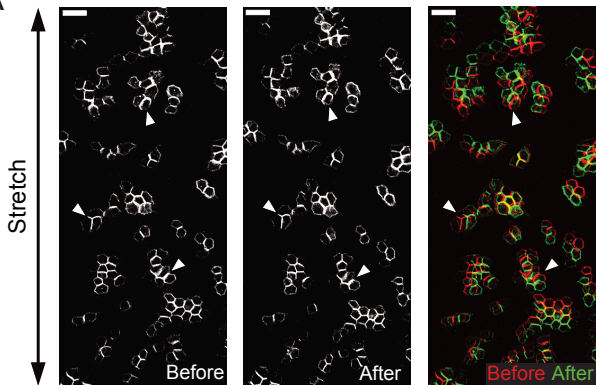
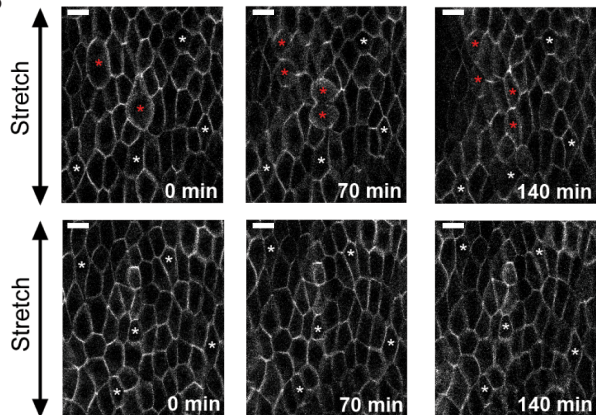
SI Video Legends

Video S1: E-cadherin-GFP-expressing cells in a non-stretched (left) and non-stretched (right) suspended monolayer. Scale bars 10 μm .

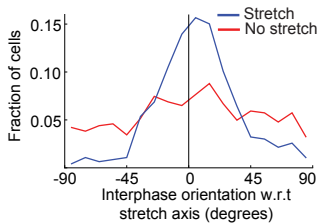
SI References

1. Harris AR, *et al.* (2012) Characterizing the mechanics of cultured cell monolayers. *Proceedings of the National Academy of Sciences of the United States of America* 109(41):16449-16454.
2. Harris AR, *et al.* (2013) Generating suspended cell monolayers for mechanobiological studies. *Nature protocols* 8(12):2516-2530.
3. Caplan MJ, *et al.* (1987) Dependence on pH of polarized sorting of secreted proteins. *Nature* 329(6140):632-635.
4. Aigouy B, *et al.* (2010) Cell flow reorients the axis of planar polarity in the wing epithelium of *Drosophila*. *Cell* 142(5):773-786.
5. Schindelin J, *et al.* (2012) Fiji: an open-source platform for biological-image analysis. *Nature methods* 9(7):676-682.
6. Jennings J (2014) A new computational model for multi-cellular biological systems. (University of Cambridge, www.repository.cam.ac.uk/handle/1810/245334).

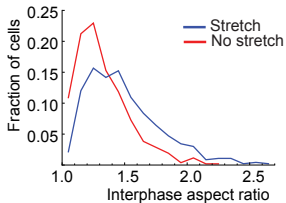


A**B**

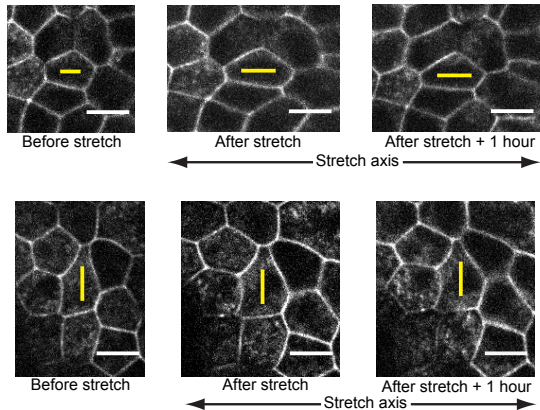
A

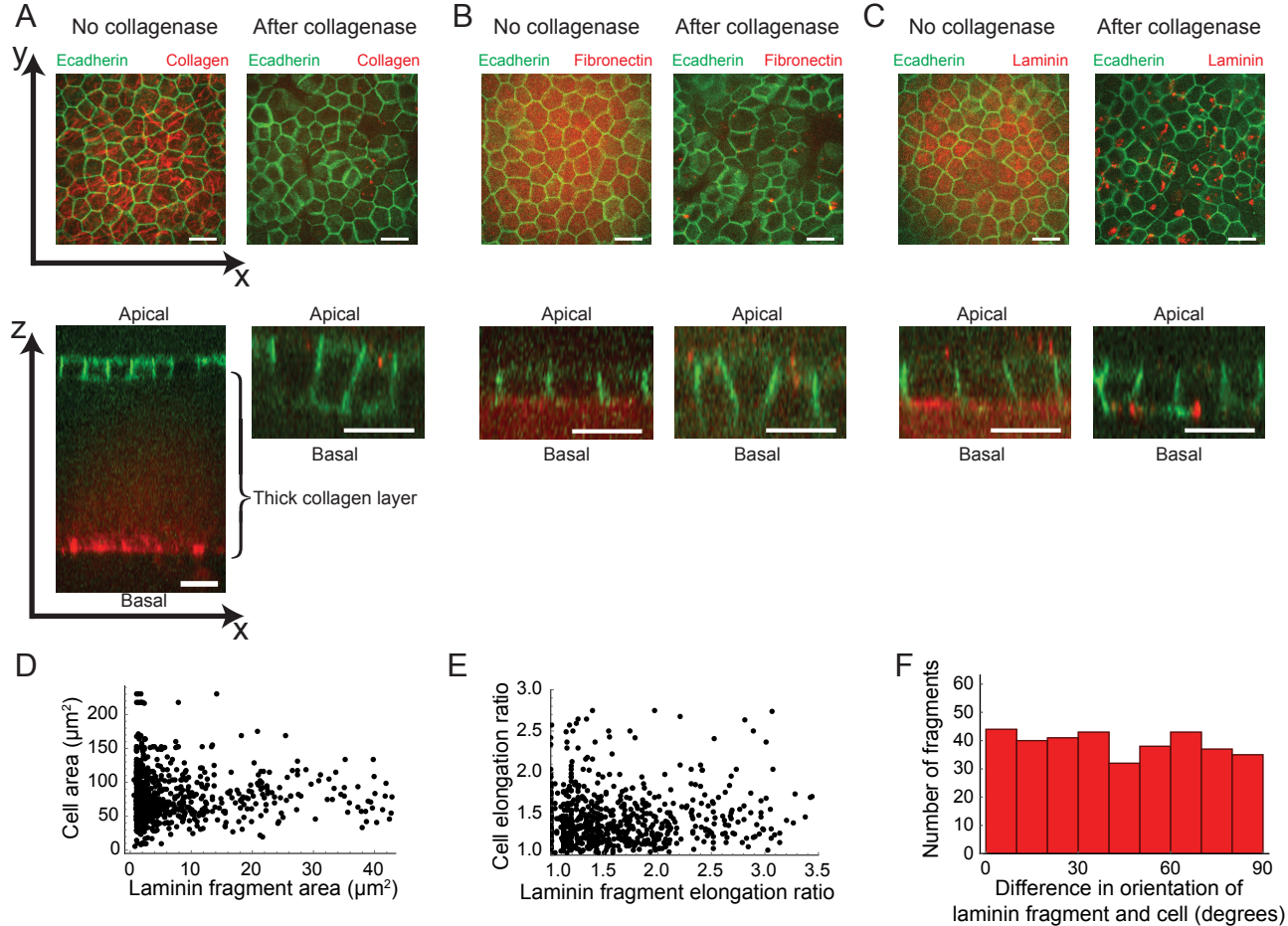


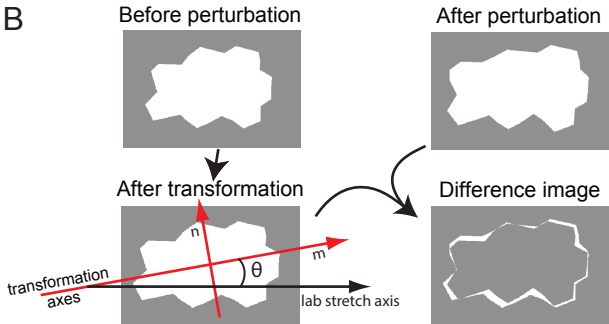
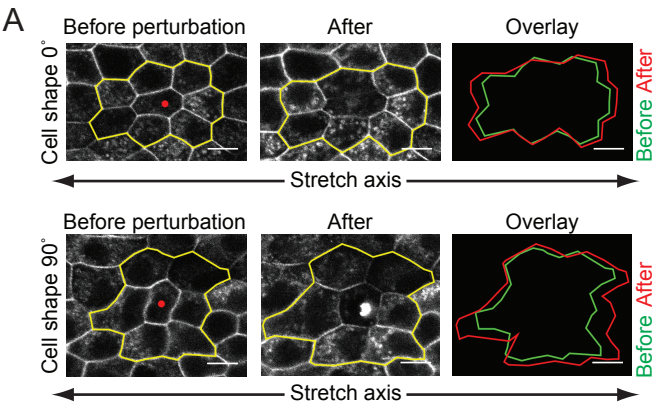
B

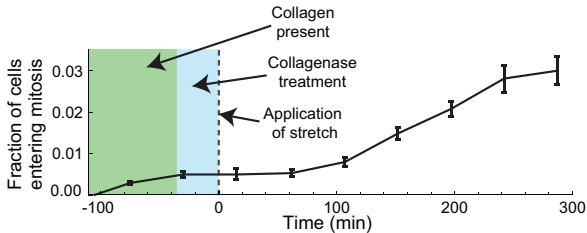
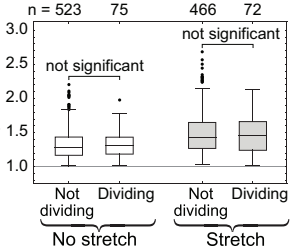
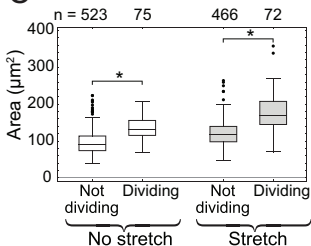


C







A**B****C**

DAPI α -tub
Actin Ecad

Stretch

Apical
side

Basal
side

